Spin injection and spin accumulation in all-metal mesoscopic spin valves

F.J. Jedema,* M.S.Nijboer, A.T. Filip,† and B.J. van Wees

Department of Applied Physics and Materials Science Center, University of Groningen,
Nijenborgh 4, 9747 AG Groningen, The Netherlands
(Dated: February 1, 2008)

We study the electrical injection and detection of spin accumulation in lateral ferromagnetic metal-nonmagnetic metal-ferromagnetic metal (F/N/F) spin valve devices with transparent interfaces. Different ferromagnetic metals, permalloy (Py), cobalt (Co) and nickel (Ni), are used as electrical spin injectors and detectors. For the nonmagnetic metal both aluminium (Al) and copper (Cu) are used. Our multi-terminal geometry allows us to experimentally separate the spin valve effect from other magneto resistance signals such as the anomalous magneto resistance (AMR) and Hall effects. We find that the AMR contribution of the ferromagnetic contacts can dominate the amplitude of the spin valve effect, making it impossible to observe the spin valve effect in a 'conventional' measurement geometry. In a 'non local' spin valve measurement we are able to completely isolate the spin valve signal and observe clear spin accumulation signals at $T = 4.2$ K as well as at room temperature (RT). For aluminum we obtain spin relaxation lengths (λ_{sf}) of 1.2 μm and 600 nm at $T = 4.2$ K and RT respectively, whereas for copper we obtain 1.0 μm and 350 nm. The spin relaxation times τ_{sf} in Al and Cu are compared with theory and results obtained from giant magneto resistance (GMR), conduction electron spin resonance (CESR), anti-weak localization and superconducting tunneling experiments. The spin valve signals generated by the Py electrodes ($\alpha_F \lambda_F = 0.5$ [1.2] nm at RT [$T = 4.2$ K]) are larger than the Co electrodes ($\alpha_F \lambda_F = 0.3$ [0.7] nm at RT [$T = 4.2$ K]), whereas for Ni ($\alpha_F \lambda_F < 0.3$ nm at RT and $T = 4.2$ K) no spin signal is observed. These values are compared to the results obtained from GMR experiments.

PACS numbers: 72.25.Ba, 72.25.Hg, 72.25.Mk, 72.25.Rb

I. INTRODUCTION

Spintronics is a rapidly emerging field in which one tries to study or make explicit use of the spin degree of freedom of the electron.[1,2,3] Sofar, the most well known examples of spintronics are the giant magneto resistance (GMR) of metallic multi-layers[4,5,6] and tunneling magneto resistance (TMR) of magnetic tunnel junctions[7,8]. Injection of hot electrons ≈ 1 eV above the Fermi energy E_F in Co/Cu (multi) layers have shown a significant spin filtering effect, enabling transistor functionality and ballistic electron magnetic microscopy.[9,10] Recent experiments have shown the ability of spin polarized currents to initiate a (local) magnetization reversal in thin ferromagnetic wires and Co/Cu multi-layer pillars[11,12,13,14,15]. A new direction is emerging, where one actually wants to inject spin currents, transfer and manipulate the spin information at the Fermi-level, and detect the resulting spin polarization in nonmagnetic metals and semiconductors. Because of spin-orbit interaction, the electron spin can be flipped and consequently a spin polarized current will have a finite lifetime. For this reason it is necessary to study spin transport in systems, where the 'time of flight' of the electrons between the injector and detector is shorter than the spin relaxation time. A first and successful attempt to electrically inject and detect spins in metals dates back to 1985 when Johnson and Silsbee successfully demonstrated spin accumulation in a single crystal aluminium bar up to temperatures of 77 K.[16,17] In their pioneering experiments they were able to observe spin precession of the induced non-equilibrium magnetization, made possible by the long spin relaxation lengths

$\lambda_{sf} > 50$ μm. In (diffusive) thin metallic films however, the spin relaxation length corresponds to typical length scales of 1 μm. We use a lateral mesosopic spin valve, to access and probe this length scale[18,19,20,21]. We note that a similar experiment using planar spin valves has been reported in Ref. 22.

In Sec. II a review of the basic model for spin transport in the diffusive transport regime is given, whereas in Sec. III this model is applied to our multi-terminal device geometry. A multi-terminal resistor model of spin injection and detection is presented in Sec. IV in order to elucidate the principles behind the reduction of the polarization of the spin current at a transparent F/N interface, also referred to as "conductivity mismatch".[23] The sample fabrication process and measurement geometry are described in Sec. V. Spin accumulation measurements in a 'conventional' and 'non-local' geometry for Py/Cu/Py and Py/Al/Py spin valves will be presented in Sec. VI and Sec. VII, whereas spin accumulation measurements on Co/Cu/Co and Ni/Cu/Ni spin valves will be presented in Sec. VIII. In Sec. IX the obtained results of Secs. VI,VII and VIII are analyzed using the model for spin transport in the diffusive regime and the results are compared to GMR, CESR, anti-weak localization and superconducting tunneling experiments.

II. THEORY OF SPIN INJECTION AND ACCUMULATION

In general, electron transport through a diffusive channel is a result of a difference in the (electro-)chemical po-

tential of two connected electron reservoirs.[24] An electron reservoir is an electron bath in full thermal equilibrium. The chemical potential μ_{ch} is by definition the energy needed to add one electron to the system, usually set to zero at the Fermi energy (this convention is adapted throughout this text), and accounts for the kinetic energy of the electrons. In the linear response regime, i.e. for small deviations from equilibrium ($|eV| < kT$), the chemical potential equals the excess electron density n divided by the density of states at the Fermi energy, $\mu_{ch} = n/N(E_F)$. In addition an electron may also have an potential energy, e.g. due to the presence of an electric field $\mathbf{E}$. The additional potential energy for a reservoir at potential V should be added to μ_{ch} in order to obtain the electrochemical potential (in the absence of a magnetic field):

$$\mu = \mu_{ch} - eV , \qquad (1)$$

where e denotes the absolute value of the electron charge.

From eq. [1] it is clear that a gradient of μ, the driving force of electron transport, can result from either a spatial varying electron density ∇n or an electric field $\mathbf{E} = -\nabla V$. Since μ fully characterizes the reservoir one is free to describe transport either in terms of diffusion ($\mathbf{E} = 0$, $\nabla n \neq 0$) or in terms of electron drift ($\mathbf{E} \neq 0$, $\nabla n = 0$). In the drift picture the whole Fermi sea has to be taken into account and consequently one has to maintain a constant electron density everywhere by imposing: $\nabla n = 0$. We use the diffusive picture where only the energy range $\Delta\mu$, the difference in the electrochemical potential between the two reservoirs, is important to describe transport. Both approaches (drift and diffusion) are equivalent in the linear regime and are related to each other via the Einstein relation:

$$\sigma = e^2 N(E_F)D , \qquad (2)$$

where σ is the conductivity and D the diffusion constant.

We focus on the diffusive transport regime, which applies when the mean free path l_e is shorter than the device dimensions. The description of electrical transport in a ferromagnet in terms of a two-current (spin-up and spin-down) model dates back to Fert and Campbell[25]. Van Son et $al.$[26] have extended the model to describe transport through ferromagnet-nonmagnetic metal interfaces. A firm theoretical underpinning, based on the Boltzmann transport equation has been given by Valet and Fert.[27] They have applied the model to describe the effects of spin accumulation and spin dependent scattering on the GMR effect in magnetic multilayers. This standard model allows for a detailed quantitative analysis of the experimental results.

An alternative model, based on thermodynamic considerations, has been put forward and applied by Johnson and Silsbee (JS)[28]. In principle both models describe the same physics, and should therefore be equivalent. However, the JS model has a drawback in that it does not

allow a direct calculation of the spin polarization of the current (η in Refs.16,28,29,30), whereas in the standard model all measurable quantities can be directly related to the parameters of the experimental system.[27,31,32]

The transport in a ferromagnet is described by spin dependent conductivities:

$$\sigma_\uparrow = N_\uparrow e^2 D_\uparrow, \text{ with } D_\uparrow = \frac{1}{3}v_{F\uparrow}l_{e\uparrow} \qquad (3)$$

$$\sigma_\downarrow = N_\downarrow e^2 D_\downarrow, \text{ with } D_\downarrow = \frac{1}{3}v_{F\downarrow}l_{e\downarrow} , \qquad (4)$$

where $N_{\uparrow,\downarrow}$ denotes the spin dependent density of states (DOS) at the Fermi energy (E_F), and $D_{\uparrow,\downarrow}$ the spin dependent diffusion constants, expressed in the spin dependent Fermi velocities $v_{F\uparrow,\downarrow}$, and electron mean free paths $l_{e\uparrow,\downarrow}$. Throughout this paper our notation is $\uparrow$ for the majority spin direction and $\downarrow$ for the minority spin direction. Note that the spin dependence of the conductivities is determined by $both$ density of states and diffusion constants. This should be contrasted with magnetic F/I/F or F/I/N tunnel junctions, where the spin polarization of the tunneling electrons is determined by the spin-dependent (local) DOS.[7,33,34] Also in a typical ferromagnet several bands (which generally have different spin dependent density of states and effective masses) contribute to the transport. However, provided that the elastic scattering time and the interband scattering times are shorter than the spin flip times (which is usually the case) the transport can still be described in terms of well defined spin up and spin down conductivities.

Because the spin up and spin down conductivities are different, the current in the bulk ferromagnet will be distributed accordingly over the two spin channels:

$$j_\uparrow = \frac{\sigma_\uparrow}{e}\frac{\partial\mu_\uparrow}{\partial x} \qquad (5)$$

$$j_\downarrow = \frac{\sigma_\downarrow}{e}\frac{\partial\mu_\downarrow}{\partial x} , \qquad (6)$$

where $j_{\uparrow\downarrow}$ are the spin up and spin down current densities. According to Eqs. 5 and 6 the current flowing in a bulk ferromagnet is spin polarized, with a polarization given by:

$$\alpha_F = \frac{\sigma_\uparrow - \sigma_\downarrow}{\sigma_\uparrow + \sigma_\downarrow}. \qquad (7)$$

The next step is the introduction of spin flip processes, described by a spin flip time $\tau_{\uparrow\downarrow}$ for the average time to flip an up-spin to a down-spin, and $\tau_{\downarrow\uparrow}$ for the reverse process. The detailed balance principle imposes that $N_\uparrow/\tau_{\uparrow\downarrow} = N_\downarrow/\tau_{\downarrow\uparrow}$, so that in equilibrium no net spin scattering takes place. As pointed out already, usually these spin flip times are larger than the momentum scattering time $\tau_e = l_e/v_F$. The transport can then be described in terms of the parallel diffusion of the two

spin species, where the densities are controlled by spin flip processes. It should be noted however that in particular in ferromagnets (e.g. permalloy[35,36,37]) the spin flip times may become comparable to the momentum scattering time. In this case an (additional) spin-mixing resistance arises[4,38,39], which we will not discuss further here.

The effect of the spin flip processes can now be described by the following equation (assuming diffusion in one dimension only):

$$D\frac{\partial^2(\mu_\uparrow - \mu_\downarrow)}{\partial x^2} = \frac{(\mu_\uparrow - \mu_\downarrow)}{\tau_{sf}}, \qquad (8)$$

where $D = D_\uparrow D_\downarrow (N_\uparrow + N_\downarrow)/(N_\uparrow D_\uparrow + N_\downarrow D_\downarrow)$ is the spin averaged diffusion constant, and the spin relaxation time τ_{sf} is given by: $1/\tau_{sf} = 1/\tau_{\uparrow\downarrow} + 1/\tau_{\downarrow\uparrow}$. We note that τ_{sf} represents the timescale over which the non-equilibrium spin accumulation $(\mu_\uparrow - \mu_\downarrow)$ decays and therefore is equal to the spin lattice relaxation time T_1 used in the Bloch equations: $\tau_{sf} = T_1$.[40] Using the requirement of current conservation, the general solution of eq. 8 for a uniform ferromagnet or nonmagnetic wire is now given by:

$$\mu_\uparrow = A + Bx + \frac{C}{\sigma_\uparrow}exp(-x/\lambda_{sf}) + \frac{D}{\sigma_\uparrow}exp(x/\lambda_{sf}) \quad (9)$$

$$\mu_\downarrow = A + Bx - \frac{C}{\sigma_\downarrow}exp(-x/\lambda_{sf}) - \frac{D}{\sigma_\downarrow}exp(x/\lambda_{sf}) \quad (10)$$

where we have introduced the spin relaxation length $\lambda_{sf} = \sqrt{D\tau_{sf}}$. The coefficients A,B,C, and D are determined by the boundary conditions imposed at the junctions where the wires are coupled to other wires. In the absence of an interface resistance and spin flip scattering at the interfaces, the boundary conditions are: 1) continuity of $\mu_\uparrow$, $\mu_\downarrow$ at the interface, and 2) conservation of spin-up and spin-down currents $j_\uparrow$, $j_\downarrow$ across the interface.

III.   SPIN ACCUMULATION IN MULTI-TERMINAL SPIN VALVE STRUCTURES

We will now apply the model of spin injection to a non local geometry, which reflects our measurement and device geometry, see Fig.1a and Fig.3c.

In our (1-dimensional) geometry we can identify 6 different regions for which Eqs. 9 and 10 have to be solved according to their boundary conditions at the interface. The geometry is schematically shown in Fig.1b, where the 6 different regions are marked with roman letters I to VI. According to Eq. 9 the equations for the spin-up electrochemical potentials in these regions, assuming parallel magnetization of the ferromagnetic regions, read:
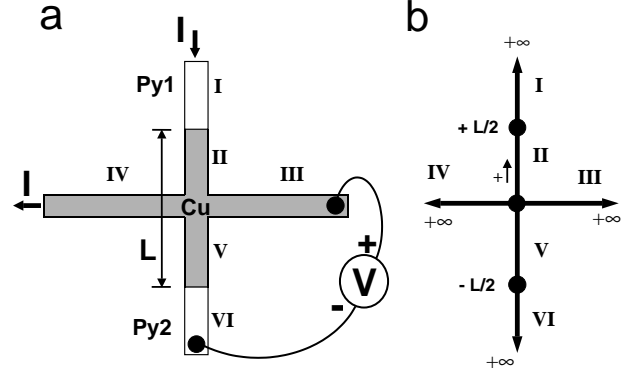

FIG. 1: (a) Schematic representation of the multi-terminal spin valve device. Regions I and VI denote the injecting (F_1) and detecting (F_2) ferromagnetic contacts, whereas regions II to V denote the four arms of a normal metal cross (N) placed in between the two ferromagnets. A spin polarized current is injected from region I into region II and extracted at region IV. (b) Diagram of the electrochemical potential solutions (Eqs. 9 and 10) in each of the six regions of the multi-terminal spin valve. The nodes represent the origins of the coordinate axis in the 6 regions, the arrows indicate the (chosen) direction of the positive x-coordinate. Regions II and III have a finite length of half the Py electrode spacing L. The other regions are semi-infinite.

$$\mu_\uparrow = A - \frac{je}{\sigma_F}x + \frac{2C}{\sigma_F(1+\alpha_F)}exp(-x/\lambda_F) \qquad (I)$$

$$\mu_\uparrow = \frac{-je}{\sigma_N}x + \frac{2E}{\sigma_N}exp(-x/\lambda_N) + \frac{2F}{\sigma_N}exp(x/\lambda_N) \quad (II)$$

$$\mu_\uparrow = \frac{2G}{\sigma_N}exp(-x/\lambda_N) \qquad (III)$$

$$\mu_\uparrow = \frac{je}{\sigma_N}x + \frac{2G}{\sigma_N}exp(-x/\lambda_N) \qquad (IV)$$

$$\mu_\uparrow = \frac{2H}{\sigma_N}exp(-x/\lambda_N) + \frac{2K}{\sigma_N}exp(x/\lambda_N) \qquad (V)$$

$$\mu_\uparrow = B + \frac{2D}{\sigma_F(1+\alpha_F)}exp(-x/\lambda_F) , \qquad (VI)$$

where we have written $\sigma_\uparrow = \sigma_F(1 + \alpha_F)/2$ and A, B, C, D, E, F, G, H and K are 9 unknown constants. The equations for the spin-down electrochemical potential in the six regions of fig. 1 can be found by putting a minus sign in front of the constants C, D, E, F, H, K, G and α_F in Eqs. I to VI. Constant B is the most valuable to extract from this set of equations, for it gives directly the difference between the electrochemical potential measured with a normal metal probe at the center of the nonmagnetic metal cross in fig.1a and the electrochemical potential measured with a ferromagnetic voltage probe at the F/N interface of region V and VI. For $\lambda_{sf} >> L$ i.e. no spin relaxation in the nonmagnetic metal of regions II

and V, the ferromagnetic voltage probe effectively probes the electrochemical potential difference between spin-up and spin-down electrons at center of the nonmagnetic metal cross. Solving the Eqs. I to VI by taking the continuity of the spin-up and spin-down electrochemical potentials and the conservation of spin-up and spin down-currents at the 3 nodes of Fig. 1b, one obtains:

$$B = -je\frac{\alpha_F^2 \frac{\lambda_N}{\sigma_N} e^{-L/2\lambda_N}}{2(M+1)[M sinh(L/2\lambda_N) + cosh(L/2\lambda_N)]} ,$$
$$(11)$$

where $M = (\sigma_F \lambda_N / \sigma_N \lambda_F)(1 - \alpha_F^2)$ and L is the length of the nonmagnetic metal strip in between the ferromagnetic electrodes. The magnitude of the spin accumulation at the F/N interface of region V and VI is given by: $\mu_\uparrow - \mu_\downarrow = B/\alpha_F$.

In the situation where the ferromagnets have an antiparallel magnetization alignment, the constant B of Eq. 11 gets a minus sign in front . Upon changing from parallel to anti-parallel magnetization configuration (a spin valve measurement) a difference of $\Delta \mu = 2B$ will be detected in electrochemical potential between the normal metal and ferromagnetic voltage probe. This leads to the definition of the so-called spin-coupled or spin-dependent resistance $\Delta R = \frac{2B}{-ejS}$, where S is the cross-sectional area of the nonmagnetic strip:

$$\Delta R = \frac{\alpha_F^2 \frac{\lambda_N}{\sigma_N S} e^{-L/2\lambda_N}}{(M+1)[M sinh(L/2\lambda_N) + cosh(L/2\lambda_N)]} . \quad (12)$$

Equation 12 shows that for $\lambda_N << L$, the magnitude of the spin signal ΔR will decay exponentially as a function of L. In the opposite limit, $\lambda_F << L << \lambda_N$ the spin signal ΔR has a 1/L dependence. In this limit and under the constraint that $ML/2\lambda_N >> 1$, we can write Eq. 12 as:

$$\Delta R = \frac{2\alpha_F^2 \lambda_N^2}{M(M+1)\sigma_N SL} . \quad (13)$$

In the situation where there are no spin flip events in the normal metal ($\lambda_N = \infty$) we find that we can write eq. 13 in an even more simple form:

$$\Delta R = \frac{2\alpha_F^2 \lambda_F^2 / \sigma_F^2}{(1 - \alpha_F^2)^2 SL/\sigma_N} . \quad (14)$$

The important point to notice is that Eq. 14 clearly shows that even in the situation when there are no spin flip processes in the normal metal, the spin signal ΔR is reduced with increasing L. The reason is that the *spin dependent* resistance ($\lambda_F/\sigma_F S$) of the injecting and detecting ferromagnets remains constant for the two spin channels, whereas the *spin independent* resistance ($L/\sigma_N S$) of

the nonmagnetic metal in between the two ferromagnets increases linearly with L. In both nonmagnetic metal regions II and V (Fig. 1) the spin currents have to traverse a total resistance path over a length $\lambda_F + L/2$ and therefore the polarization of the current flowing through these regions will decrease linearly with L and hence the spin signal ΔR. Note that in the regions V and VI no net current is flowing as the opposite flowing spin-up and spin-down currents are equal in magnitude.

Using Eqs. 5, 6 and I we can calculate the current polarization *at the interface* of the current injecting contact, defined as $P = \frac{j_\uparrow^{int} - j_\downarrow^{int}}{j_\uparrow^{int} + j_\downarrow^{int}}$. We obtain:

$$P = \alpha_F \frac{Me^{L/2\lambda_N} + 2cosh(L/2\lambda_N)}{2(M+1)[M sinh(L/2\lambda_N) + cosh(L/2\lambda_N)]} .$$
$$(15)$$

In the limit that $L >> \lambda_N$ we obtain the polarization of the current at a single F/N interface:[26]

$$P = \frac{\alpha_F}{M+1} . \quad (16)$$

Again, Eq. 16 shows a reduction of the polarization of the current at the F/N interface, when the spin dependent resistance ($\lambda_F/\sigma_F S$) is much smaller that the spin independent resistance ($\lambda_N/\sigma_N S$) of the nonmagnetic metal. This situation becomes progressively worse for a semiconductor as σ_N is reduced by a factor of 100 or more and has become known as the "conductivity mismatch".[23,41]

Finally we note that the spin signal ΔR^{Conv} can also be calculated for a conventional measurement geometry, see Fig. 3b, writing down similar equations and boundary conditions as we have done for the non local geometry (Eqs. I to VI). We find:

$$\Delta R^{Conv} = 2\Delta R . \quad (17)$$

Equation 17 shows that the magnitude of the spin valve signal measured with a conventional geometry is increased with a factor two as compared to the non local spin valve geometry (see also Ref. 31 Eq. 45).

IV. RESISTOR MODEL OF MULTI-TERMINAL SPIN VALVE STRUCTURES

More physical insight can be gained by considering an equivalent resistor network of the spin valve device.[42] In the linear transport regime, where the measured voltages are linear functions of the applied currents, the spin transport for the conventional and non local geometry can be represented by a two terminal and four terminal resistor network respectively. This is shown in Fig. 2 for both parallel and anti-parallel configuration of the ferromagnetic electrodes. The resistances $R_\downarrow$ and $R_\uparrow$

Conventional

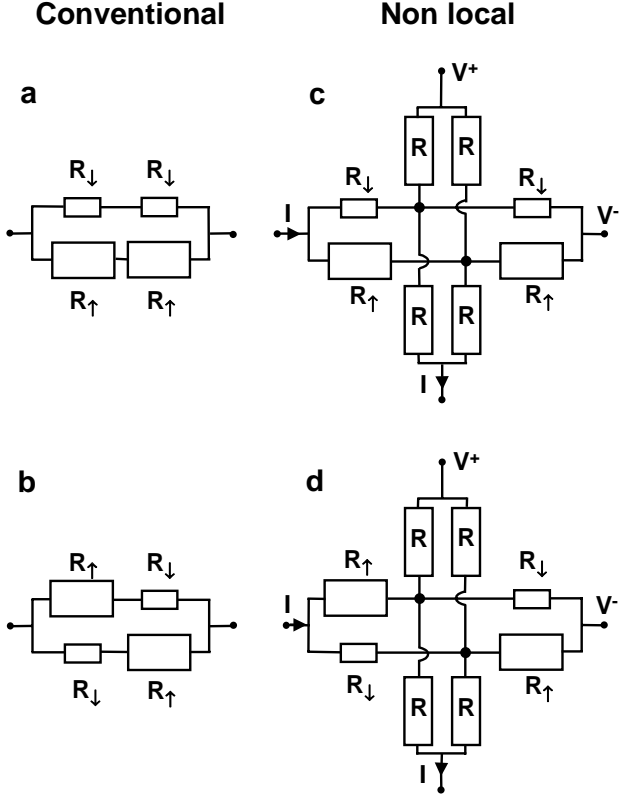**Non local**

a

c

b

d

FIG. 2: The equivalent resistor networks of the spin valve device. (a) The conventional spin valve geometries in parallel and (b) in anti-parallel configuration. (c) The non-local spin valve geometry in parallel and (d) in anti-parallel configuration.

represent the resistances of the spin up and spin down channels, which consists of the different spin-up and spin-down resistance of the ferromagnetic electrodes ($R_\uparrow^F, R_\downarrow^F$) and the spin independent resistance R^N of the nonmagnetic wire in between the ferromagnetic electrodes. From resistor model calculations we obtain:

$$R_\uparrow = R_\uparrow^F + R^N = \frac{2\lambda_F}{w(1+\alpha_F)}R_\square^F + \frac{L}{w}R_\square^N \quad (18)$$

$$R_\downarrow = R_\downarrow^F + R^N = \frac{2\lambda_F}{w(1-\alpha_F)}R_\square^F + \frac{L}{w}R_\square^N , \quad (19)$$

where $R_\square^F = 1/\sigma_F h$ and $R_\square^N = 1/\sigma_N h$ are the "square" resistances of the ferromagnet and non-magnetic metal thin films, w and h are the width and height of the nonmagnetic metal strip. The resistance $R = (\lambda_N - L/2)2R_\square^N/w$ in Fig. 2c and Fig. 2d represents the resistance for one spin channel in the side arms of the nonmagnetic metal cross over a length $\lambda_N - L/2$, corresponding to the regions IV and V of Fig. 1b.

Provided that $\lambda_N \gg L$ the spin dependent resistance ΔR^{Conv} between the parallel (Fig. 2a) and anti-parallel (Fig. 2b) resistor networks for the conventional geometry

can be calculated using eqs. 18 and 19. We obtain the familiar expression:[4,6]

$$\Delta R^{Conv} = \frac{(R_\downarrow - R_\uparrow)^2}{2(R_\uparrow + R_\downarrow)}. \quad (20)$$

For the non local geometry and under the condition $\lambda_N \gg L$ the spin dependent resistance ΔR between the parallel (Fig. 2c) and anti-parallel (Fig. 2d) resistor network can also be calculated. We obtain:

$$\Delta R = \frac{(R_\downarrow - R_\uparrow)^2}{4(R_\uparrow + R_\downarrow)}. \quad (21)$$

Equation 21 again shows that the spin signal measured in a non local geometry is reduced by a factor 2 as compared to a conventional measurement. Provided that $R_\uparrow^F, R_\downarrow^F \ll R^N$ we can use Eqs. 18 and 19 to rewrite Eq. 21 into:

$$\Delta R = \frac{2\alpha_F^2 \lambda_F^2 R_\square^{F2}}{(1-\alpha_F^2)^2 L w R_\square^N} . \quad (22)$$

Using $S = wh$ and replacing the square resistance by the conductivities Eq. 22 reduces to Eq. 14. A direct relation can now be obtained between the experimentally measured quantities ΔR, $R_\square^N$, $R_\square^F$ and the relevant spin dependent properties of the ferromagnet:

$$R_\downarrow - R_\uparrow = \sqrt{8\Delta R R_\square^N \frac{L}{w}} = \frac{4\alpha_F \lambda_F R_\square^F}{(1-\alpha_F^2)w}. \quad (23)$$

V. SAMPLE FABRICATION AND MEASUREMENT GEOMETRY

We use permalloy $Ni_{80}Fe_{20}$ (Py), cobalt (Co) and nickel (Ni) electrodes to drive a spin polarized current into copper (Cu) or (Al) crossed strips. Different aspect ratios of the rectangular ferromagnetic injector (F1) and detector strips (F2) result in different switching fields of the magnetization reversal process, allowing control over the relative magnetization configuration of F1 and F2 (parallel/anti-parallel) by applying a magnetic field parallel to the long axis of the ferromagnetic electrodes.[43,44] Two sets [F1,F2] of different sizes are used in the experiments. One set has dimensions of 2×0.8 μm^2 (F1) and 14×0.5 μm^2 (F2), whereas the other set has dimensions of 2×0.5 μm^2 (F1) and 14×0.15 μm^2 (F2). An example of a typical device is shown in Fig. 3.

The devices are fabricated in two steps by means of conventional e-beam lithography with PMMA resist and lift-off technique. To avoid magnetic fringe fields, the ferromagnetic electrodes are deposited first on a thermally oxidized silicon substrate. The 40 nm thick Py
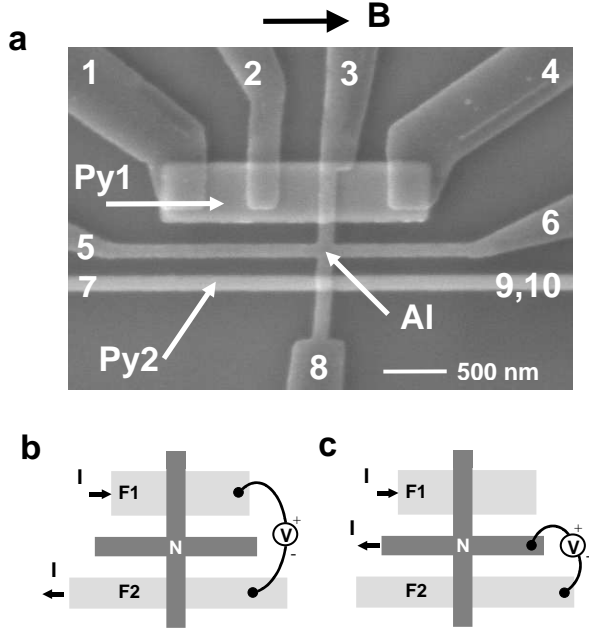
FIG. 3: a, Scanning electron microscope (SEM) picture of the lateral mesoscopic spin valve device with a ferromagnetic electrode spacing $L = 500$ nm. The two horizontal strips are the ferromagnetic electrodes F1 (Py1) and F2 (Py2). Their sizes are $(2 \times 0.5 \ \mu m^2)$ and $(14 \mu m \times 0.15 \mu m^2)$ respectively. An aluminum (Al) cross is placed in between the Py electrodes, which vertical arms lay on top of the Py electrodes. A total of 10 contacts (not all visible) are connected to the device. b, The conventional measurement geometry and (c) the non local measurement geometry. The black arrow indicates the direction of the applied magnetic field B in the measurements.

electrodes are sputter deposited on a 2 nm tantalum (Ta) adhesion layer. The base pressure of the sputter system was $2 \cdot 10^{-8}$ mbar vacuum, whereas the background Ar pressure during sputtering was 1 mbar. A small B-field of 3 mT along the long axis of the Py electrodes was applied during growth in order to align the magneto crystalline anisotropy with the magnetic shape anisotropy of Py electrode. The conductivity of the Py film was determined to be $\sigma_{Py} = 6.6 \cdot 10^6 \ \Omega^{-1} m^{-1}$ and $\sigma_{Py} = 1.2 \cdot 10^7 \ \Omega^{-1} m^{-1}$ at RT and 4.2 K respectively. The 40 nm thick Co (99.95 % *pure*) and 30 nm thick Ni (99.98 % *pure*) electrodes were deposited by e-gun evaporation in a $1 \cdot 10^{-6}$ mbar vacuum (base pressure: $2 \cdot 10^{-7}$ mbar). The conductivities of the Co and Ni films were determined to be $\sigma_{Co} = 4.2 \cdot 10^6 \ \Omega^{-1} m^{-1}$ and $\sigma_{Ni} = 7.6 \cdot 10^6 \ \Omega^{-1} m^{-1}$ at RT, whereas at 4.2 K they were $\sigma_{Co} = 7.3 \cdot 10^6 \ \Omega^{-1} m^{-1}$ and $\sigma_{Ni} = 1.6 \cdot 10^7 \ \Omega^{-1} m^{-1}$. In the second fabrication step, 50 nm thick crossed Cu (99.99 % *pure*) or Al (99.999 % *pure*) strips were deposited by e-gun evaporation in a $1 \cdot 10^{-8}$ mbar vacuum (base pressure: $2 \cdot 10^{-9}$ mbar). Prior to the Cu or Al deposition, a few nm of Py, Co or Ni material was removed from the ferromagnetic electrodes by Kaufmann sputtering at

500 Volt for 30 seconds in a $2 \cdot 10^{-4}$ mbar Ar pressure, thereby removing the oxide to ensure transparent contacts. The time in between the Kaufmann sputtering and Cu or Al deposition was about 3 minutes. The conductivities of the Cu and Al films were determined to be $\sigma_{Cu} = 3.5 \cdot 10^7 \ \Omega^{-1} m^{-1}$ and $\sigma_{Al} = 3.1 \cdot 10^7 \ \Omega^{-1} m^{-1}$ at RT, whereas at 4.2 K they were $\sigma_{Cu} = 7.1 \cdot 10^7 \ \Omega^{-1} m^{-1}$ and $\sigma_{Al} = 8.0 \cdot 10^7 \ \Omega^{-1} m^{-1}$.

Two different measurement geometries are used to measure the spin valve effect in our device structure, the so called 'conventional' geometry (Fig.3b) and 'non-local' geometry (Fig.3c). In the conventional measurement geometry the current is sent from contact 1 to 7 and the signal $R = V/I$ is measured between contacts 4 and 9, see Fig. 3a. The conventional geometry suffers from a relatively large background resistance as compared to the spin valve resistance. Small parts of the ferromagnetic electrodes underneath the vertical Cu or Al wires of the cross are included in this background resistance, which can give rise to AMR[45] contributions and Hall effects. In the non-local measurement geometry the current is sent from contact 1 to 5 and the signal $R = V/I$ is measured between contacts 6 and 9. This technique is similar to the "potentiometric" method of Johnson used in Ref. 29,30. However, the separation of the current and voltage circuits, allow us to remove the AMR contribution and Hall effecs of the ferromagnetic electrodes completely: the (magneto) resistance of the current injecting contact (F1) is not relevant because any voltage drop that develops across it will not influence the current that is sent through it and similarly, no current flows through the ferromagnetic voltage contact (F2), so its (magneto) resistance does not effect the voltage measurement. Therefore the only region which could possibly give rise to a magneto resistance signal is the nonmagnetic metal cross, but explicit measurements confirm that this region does not produce any magneto resistance. Moreover, this central region would be unable to produce a Hall signal in a non local measurement with a magnetic field perpendicular to the substrate plane as both voltage probes are attached longitudinal to the direction the current.

VI. SPIN ACCUMULATION IN PY/CU/PY SPIN VALVES

The measurements were performed by standard ac-lock-in-techniques, using current magnitudes of 100 μA to 1 mA. Typical spin valve signals of two samples MSV1 and MSV2 (of the same batch) with a Py electrode spacing of $L = 250$ nm are shown in the Figs. 4,5 and 6. They are both measured in a non local measurement geometry and conventional measurement geometry. Sample MSV1, data shown in Fig. 4 and 5, had a current injector Py1 electrode of size $2 \times 0.5 \ \mu m^2$, whereas the detector electrode Py2 had a size of $14 \times 0.15 \ \mu m^2$. Sample MSV2, data in shown Fig. 6, had wider Py electrodes of $2 \times 0.8 \ \mu m^2$ and $14 \times 0.5 \mu m^2$. The first set of (nar-

rower) Py electrodes [Py1,Py2] had a more ideal switching behavior and had three times larger switching fields as compared to the second Set [Py1,Py2]. We note that a discussion of the magnetic behavior of the Py electrodes and contacts has been given in Ref. 19. To control the parallel/anti-parallel magnetization configuration of the Py electrodes a magnetic field is applied parallel to the long (easy) axis of the Py electrodes.

A.   Non local spin valve geometry

Figure 4a and 4b show typical data in the non local measurement geometry taken at 4.2 K and RT for sample MSV1 with a 250 nm Py electrode spacing. Sweeping the magnetic field from negative to positive field, an increase in the resistance is observed, when the magnetization of Py1 flips at 9 mT, resulting in an anti-parallel magnetization configuration. The rise in resistance is due to the spin accumulation or equivalently an excess spin density present in the Cu metal. When the magnetization of Py2 flips at 47 mT ($T = 4.2$ K) and 38 mT (RT), the magnetizations are parallel again, but now point in the opposite direction. The magnitude of the measured background resistance, around 30 $m\Omega$ at $T = 4.2$ K and 120 $m\Omega$ at RT, depends on the geometrical shape of the Cu cross and is typically a fraction of the Cu square resistance.

Figure 4c and 4d show the "memory effect". Coming from high positive B field, the sweep direction of the B field is reversed after Py1 has switched, but Py2 has not. At the moment of reversing the sweep direction, the magnetic configuration of Py1 and Py2 is anti-parallel, and accordingly a higher resistance is measured. When the B-field is swept back to its original high positive value, the resistance remains at its increased level until Py1 switches back at a positive field of 9 mT. At zero B field the resistance can therefore have two distinct values, depending on the history of the Py electrodes.

B.   Conventional spin valve geometry

The top curve in Fig. 5 shows the magneto resistance behavior of sample MSV1 in the conventional measurement geometry. A small AMR contribution (dip in curve) of the Py1 electrode around -9 mT and a small Hall signal caused by the Py2 electrode can be observed in the negative sweep direction. Because a small part of the Py electrodes underneath the Cu wire is measured in this geometry, (local) changes in the magnetization at the Py/Cu contact area can produce an AMR or Hall signal.[19] In the positive sweep direction a dip is no longer observed indicating that the magnetization reversal of the Py1 electrode is not the same for the two sweep directions. However, in the magnetic field range in between the two switching fields, we do observe a resistance 'plateau' from 10 mT up to a field of 45 mT.
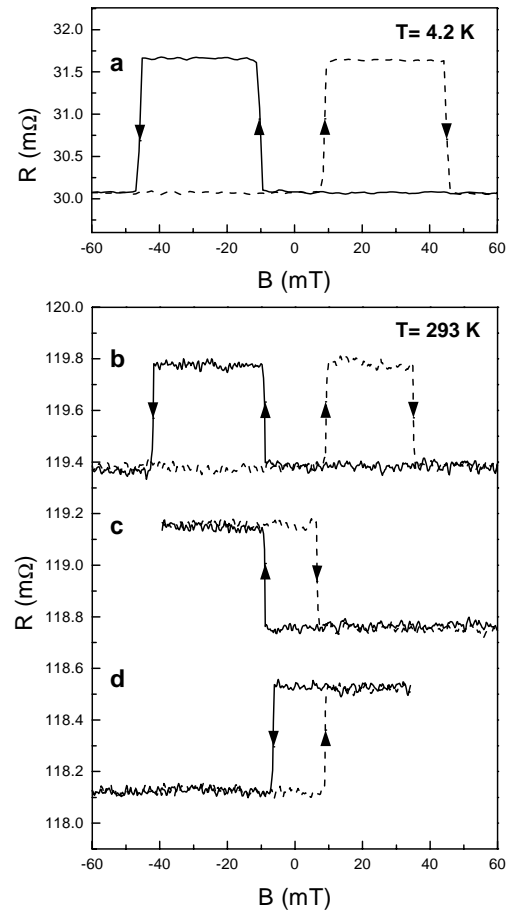

FIG. 4: The spin valve effect at $T = 4.2$ K (a) and RT (b) in the non-local geometry for a Py/Cu/Py spin valve device (sample MSV1) with 250 nm Py electrode spacing. An increase in resistance is observed, when the magnetization configuration is changed from parallel to anti-parallel. The solid (dashed) lines correspond to the negative (positive) sweep direction. (c),(d) illustrate the "memory effect". For clarity the (c) and (d) are off set downwards. Note that the vertical scale of (a) is different from (b),(c) and (d). The sizes of the Py1 and Py2 electrodes are 2×0.5 μm^2 and $14\mu m \times 0.15\mu m^2$

The magnitude of the spin valve effect measured in the conventional geometry is about 4.1 $m\Omega$ at $T = 4.2$. This is about 2.5 times bigger than the magnitude of the spin signal measured in a 'non-local geometry (1.6 $m\Omega$). Note that the factor 2.5 is deviating from the factor 2 as predicted by the eq. 17. This is attributed to deviations from our 1-dimensional model, which can be expected for the samples with the shortest Py electrode spacing $L = 250$ nm, as the presence of the Cu side arms for these samples, see Fig. 3, are most felt.

The top curve in Fig. 6 shows the magneto resistance behavior in the conventional measurement geometry for the sample MSV2. Here a change of the resistance is already observed before the field has reached zero in a positive field sweep, whereas the negative field sweep is very asymmetrical compared to the positive field sweep.
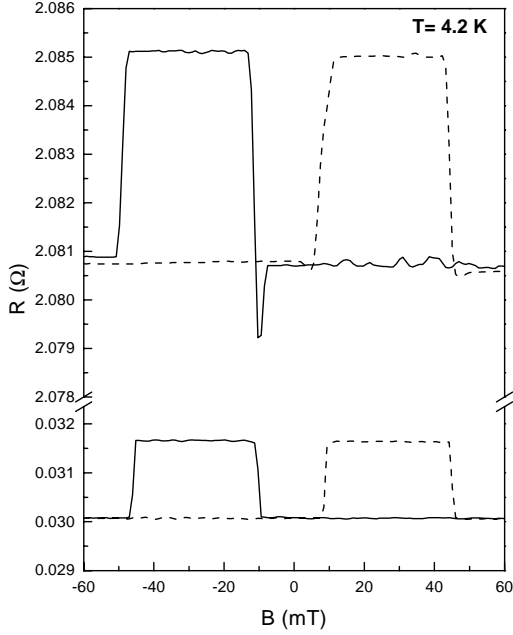
FIG. 5: The spin valve effect of sample MSV1 in a conventional measurement geometry (top curve) at $T = 4.2$ K and non-local measurement geometry (bottom curve), with a Py electrode spacing $L = 250$ nm. The sizes of the Py electrodes are 2×0.5 μm^2 (Py1) and 14×0.15 μm^2 (Py2). The solid(dotted) curve corresponds with a negative (positive) sweep direction of the B-field.
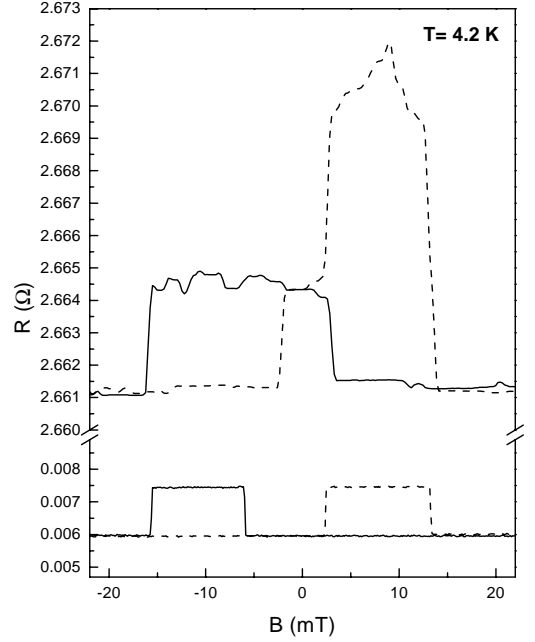

FIG. 6: The spin valve effect of sample MSV2 in a conventional measurement geometry (top curve) at $T = 4.2$ K and non-local measurement geometry (bottom curve), with a Py electrode spacing $L = 250$ nm. The sizes of the Py electrodes are 2×0.8 μm^2 (Py1) and 14×0.5 μm^2 (Py2). The solid(dotted) curve corresponds with a negative (positive) sweep direction of the B-field.

This is attributed to the formation of a multi-domain structure in the 2×0.8 μm^2 (Py1) electrode, causing a large AMR (≈ 10 $m\Omega$) signal at the Py/Cu contact area of the Py1 electrode.

However, in a non local measurement geometry, the "contact" magneto resistance contribution of the Py electrodes can be removed and a clear spin valve signal is observed with a similar magnitude as sample MSV1. This is shown in the bottom curve of Fig. 6. Note also that the larger widths and aspect ratio of the Py electrodes in sample MSV2 result in three times smaller switching fields as compared to sample MSV1.

C. Dependence on Py electrode spacing

A reduction of the magnitude of spin signal ΔR is observed with increased electrode spacing L, as shown in Fig. 7. By fitting the data to Eq. 12 we have obtained the spin relaxation length λ_N in the Cu wire. From the best fits we find a value of 1 μm at $T = 4.2$ K, and 350 nm at RT. These values are compatible with those reported in literature, where 450 nm is obtained for Cu in GMR measurements at 4.2 K.[46] However a detailed discussion on the obtained spin relaxation lengths and corresponding spin relaxation times will be given in Sec. IX.

In principle the fits of Fig. 7 also yield the spin polarization α_F and the spin flip length λ_F of the Py electrodes. However, the values of α_F and λ_F cannot be determined separately, as in the relevant limit ($M \gg 1$) which applies to the Py/Cu/Py experiments ($12 < M < 26$), the spin signal ΔR is proportional to the product $\alpha_F \lambda_F$ as is shown by Eq. 14. From the fits we find that $\alpha_F \lambda_F = 1.2$ nm at 4.2 K and $\alpha_F \lambda_F = 0.5$ nm at RT. Taking, from literature[35,36,37], a spin flip length in the Py electrode of $\lambda_F = 5$ nm (at 4.2 K), a bulk current polarization of ≈ 20 % in the Py electrodes at $T = 4.2$ K is obtained: $\alpha_F = 0.2$. We note however that the injected spin polarized current from the Py electrode is partially shunted by the Cu wire lying on top of the Py electrode. When taken into account we estimate that it could increase the value $\alpha_F \lambda_F$ by a factor 2 to 3.

It is also possible to calculate the polarization of the current at the Py/Cu interface. For a sample with a Py electrode spacing of $L = 250$ nm at $T = 4.2$ K and using Eq. 15 we find: $P \simeq 0.02$, a factor 10 lower than the bulk polarization α_F of the Py electrodes. From the resistor model we can see why the current polarization at the Py/Cu interface is reduced. For this we need to calculate the magnitude of the spin dependent resistance difference. Using Eq. 23 and $L = 250$ nm, $\Delta R = 1.6$ $m\Omega$, $R_{\square}^N = 0.3$ Ω and $w = 100$ nm (at $T = 4.2$ K) we find: $R_\downarrow - R_\uparrow \approx 100$ $m\Omega$. From the right hand side term of Eq.
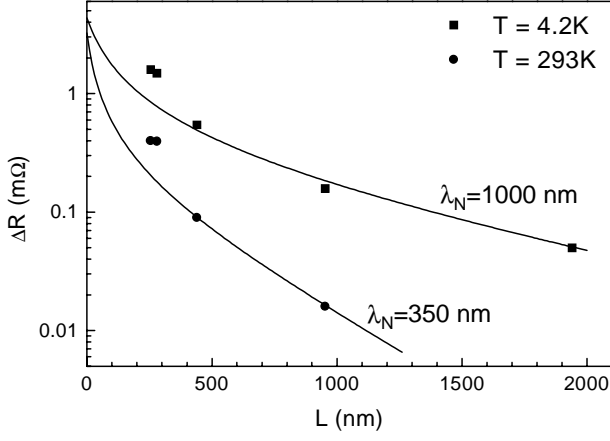
FIG. 7: Dependence of the magnitude of the spin signal ΔR on the Py electrode distance L, measured on Py/Cu/Py samples in the non local geometry. The solid squares represent data taken at $T = 4.2$ K, the solid circles represent data taken at RT. The solid lines represent the best fits based on equation 12.

23 and using $R_\square^F = 2$ Ω we can check that this indeed corresponds with the value of $\alpha_F \lambda_F \approx 1.2$ nm, as was also obtained from the fit in Fig. 7. From Eqs. 18, 19 and using $\lambda_F = 5$ nm, $\alpha_F = 0.2$ (at 4.2 K) we obtain the spin up and spin down resistance of the Py ferromagnet:

$$R_\uparrow^{Py} = \frac{2\lambda_F}{w(1+\alpha_F)} R_\square^F \approx 160 \ m\Omega \qquad (24)$$

$$R_\downarrow^{Py} = \frac{2\lambda_F}{w(1-\alpha_F)} R_\square^F \approx 260 \ m\Omega \ . \qquad (25)$$

This shows that the total resistance experienced over a length $\lambda_F + \lambda_N$ by the spin up and spin down currents is indeed dominated by the spin *independent* resistance $R^N + R = \lambda_N 2R_\square^N/w \simeq 6$ Ω. Here we have used that $\lambda_N = 1$ μm at $T = 4.2$ K and $w = 100$ nm. This leads to a interface polarization of $P \approx (R_\downarrow - R_\uparrow)/(R^N + R) \approx 2\%$ at the Py/Cu interface.

All though the role of interface resistance for spin injection will be described in the next section, we note here that the small difference $R_\downarrow - R_\uparrow \approx 100$ $m\Omega$ responsible for a spin valve signal of $\Delta R = 1.6$ $m\Omega$ could possibly also result from an interface resistance at the Py/Cu interface. Commonly reported resistivities of $5 \cdot 10^{-16}$ Ωm^2 for the Py/Cu interface[35,36,37,42,47] and a contact area of $S = 1 \cdot 10^{-14}$ m^2 (i.e. $R_{int} = 50$ $m\Omega$) would yield a realistic interface polarization of $\eta = 0.5$ for the Py/Cu interface, using eq. 26. However, the specific details of the spin injection mechanism (interface, bulk or a combination) do not alter the conclusion that the total spin dependent resistance $R_\downarrow - R_\uparrow \approx 100$ $m\Omega$ is dominated by the spin independent resistance of the Cu strip over a spin relaxation length and hence leads to a considerable reduction of the spin valve signal, as was pointed out above.

D. Comparison with Johnson Spin Transistor

The magnitude of the spin signals in the Py/Cu/Py samples, when scaled to the cross sections utilized in the Au thin film devices of Ref. 29,30 (the "Johnson spin transistor"), are more than 10^4 times smaller than obtained in that previous work. However, in that earlier work it was necessary to invoke a spin polarization exceeding 100% to explain the results in terms of spin accumulation.[29,30] This contrasts our results, which yield a spin polarization P of the current injected in the Cu wire at the Py/Cu interface of about $1-2\%$.

In Refs. 29,30,48 and 49 Johnson postulates that spin injection is mediated by interfacial transport, because the interface resistances $R_\uparrow^{int}$, $R_\downarrow^{int}$ would dominate the total resistance in both spin-up and spin-down channels: $R_\uparrow^{int} > R_\uparrow^F + R^N + R$ and $R_\downarrow^{int} > R_\downarrow^F + R^N + R$ respectively. In this limit spin injection would be characterized by the interfacial spin injection parameter defined as:

$$\eta = \frac{R_\downarrow^{int} - R_\uparrow^{int}}{R_\uparrow^{int} + R_\downarrow^{int}} \ , \qquad (26)$$

and Johnson derives the following expression for the spin accumulation signal[30,48]:

$$\Delta R = \frac{2\eta^2 \lambda_N^2}{\sigma_N SL} \ . \qquad (27)$$

Applying Eq. 27 Johnson calculates an expected spin signal of $\Delta R = 1.9$ Ω for our device with the shortest Py electrode spacing $L = 250$ nm, using $S = 5 \cdot 10^{-15}$ m^2, $\sigma_{Cu} = 7.1 \cdot 10^7$ $\Omega^{-1}m^{-1}$, $\eta = 0.4$ and $\lambda_N = 1.0$ μm.[48]

However a polarization of the current at the Py/Cu interface of $\eta = 40$ % would require spin dependent interface resistances of $R_\uparrow^{int} = 16$ Ω and $R_\downarrow^{int} = 37$ Ω, using Eqs. 26, 21 and replacing Eqs. 18 and 19 by:

$$R_\uparrow = R_\uparrow^{int} + R_\uparrow^F + R^N \qquad (28)$$

$$R_\downarrow = R_\downarrow^{int} + R_\downarrow^F + R^N \ , \qquad (29)$$

where the spin dependent interface resistances $R_\uparrow^{int}$ and $R_\downarrow^{int}$ have simply been added up to bulk spin dependent resistances $R_\uparrow^F$ and $R_\downarrow^F$ because the spin polarization η as well as the bulk spin polarization α_F are found to be positive ($\alpha_F > 0$ and $\eta > 0$) for Py and Cu.[35,36,37,50] The values $R_\uparrow^{int} = 16$ Ω and $R_\downarrow^{int} = 37$ Ω yield a total single interface resistance $R_{int} = 11$ Ω or equivalently, a interface resistivity of $1 \cdot 10^{-13}$ Ωm^2. This is more than a 100 times larger then the upper limit 0.1 Ω or equivalently a contact resistivity of $1 \cdot 10^{-15}$ Ωm^2 that we are able to determine from our experiment, see Figs. 5 and 6.

The above arguments also apply for the experiment of Refs. 29,30 where a gold layer is sandwiched in between two Py layers. There is no physical reason why

there should exist an interface resistivity larger than $1 \cdot 10^{-13} \ \Omega m^2$ between the Au and Py or Co layers in the experiment of Ref. 29, which can explain an interface current polarization of $\eta = 0.4$ or more. Equation 27 can therefore not be applied to the experiment of Ref. 29, because it does not include the (fast) spin relaxation reservoirs of the ferromagnetic injector and detector contacts, which dominate the total spin relaxation in the case of transparent contacts, as was already pointed out in Refs. 31,32.

In view of this, given the unexplained discrepancies ($\eta > 3$) of the earlier work in Ref. 29,30, and the more consistent values obtained in the recent work, it is our opinion that the results of Refs. 29,30 cannot be reconciled with spin injection and spin accumulation.

VII. SPIN ACCUMULATION IN PY/AL/PY SPIN VALVES

Here we will describe spin injection experiments using permalloy $Ni_{80}Fe_{20}$ (Py) strips as ferromagnetic electrodes to drive a spin polarized current via transparent contacts into aluminum (Al) crossed strips, see Fig. 3. Similar current polarizations and spin relaxation lengths for Py and Al are obtained as in the previous section (Sec. VI).

A. Spin valve measurements

Figure 8 shows a typical spin valve signal of a Py/Al/Py sample with a Py separation spacing of $L = 250$ nm and Py electrodes of sizes $2 \times 0.8 \ \mu m^2$ and $14 \times 0.5 \ \mu m^2$.

The top curve in Fig. 8 shows the magneto resistance behavior in the conventional measurement geometry. Again the magneto resistance signals of the Py contacts are dominating in this geometry, reaching a maximal amplitude of about 6 $m\Omega$. Note that the two resistance values at high positive and negative field differ by a value of about 0.3 $m\Omega$, which is attributed to a local hall effect caused by the $14 \times 0.5 \ \mu m^2$ Py electrode. The bottom curves in Fig. 8 show magnetic field sweeps in the non local measurement geometry, which clearly shows a spin valve signal having removed all the spurious contact magneto resistance effects. The magnitude of the spin valve signal measured is 0.18 $m\Omega$ at 4.2 K.

B. Dependence on Py electrode spacing

A reduction of the magnitude of spin signal ΔR of the Py/Al/Py samples is observed with increased electrode spacing L, as shown in Fig. 9. However, for the $T = 4.2$ K data this dependence is not monotonic. The spin valve devices with small $L = 250$ nm and $L = 500$ nm show a smaller spin valve signal than the device with $L = 1 \ \mu m$.
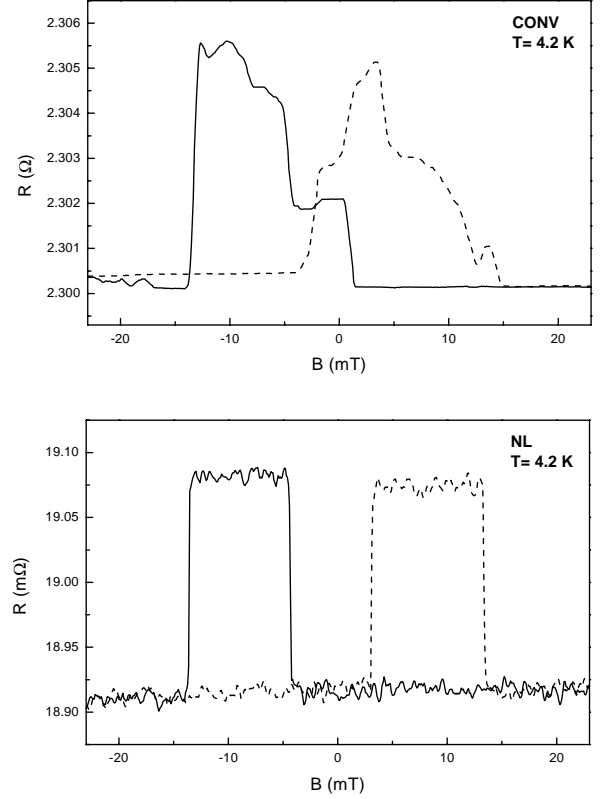

FIG. 8: The spin valve effect of a Py/Al/Py sample using a conventional measurement geometry (CONV, top curve) at $T = 4.2$ K and non-local measurement geometry (NL, bottom curve), with a Py electrode spacing $L = 250$ nm. The sizes of the Py electrodes are $2 \times 0.8 \ \mu m^2$ (Py1) and $14 \times 0.5 \ \mu m^2$ (Py2). The solid(dotted) curve corresponds with a negative (positive) sweep direction of the B-field.

We note that all the devices shown in Fig. 9 are from the same (processing) batch. However, the granular structure of the Al film with a grain size in the order of the width of the Al strip causes fluctuations in the resistance of the Al strip in between the Py electrodes. The sample with $L = 250$ nm and $L = 500$ nm indeed show a higher resistance than expected when measured in the conventional geometry at $T = 4.2$ K. This irregular behavior of the resistance due to grains is not observed at Rt due to the additional presence of phonon scattering. From the best fits to Eq. 12 we find a spin relaxation length λ_N in Al of 1.2 μm at $T = 4.2$ K and 600 nm at RT. Note that the spin flip lengths are about 2 times larger than reported in Ref. 20. The reason for this increase is the higher conductivity of the Al in these samples, caused by a lower background pressure of $1 \cdot 10^{-8}$ mbar during evaporation as compared to a background pressure of $1 \cdot 10^{-6}$ used in Ref. 20.

The fits of Fig. 9 also yield the spin polarization α_F and the spin flip length λ_F of the Py electrodes. We find $\alpha_F \lambda_F = 1.2$ nm at 4.2 K and $\alpha_F \lambda_F = 0.5$ nm at RT, in agreement with the Py/Cu/Py spin valve data
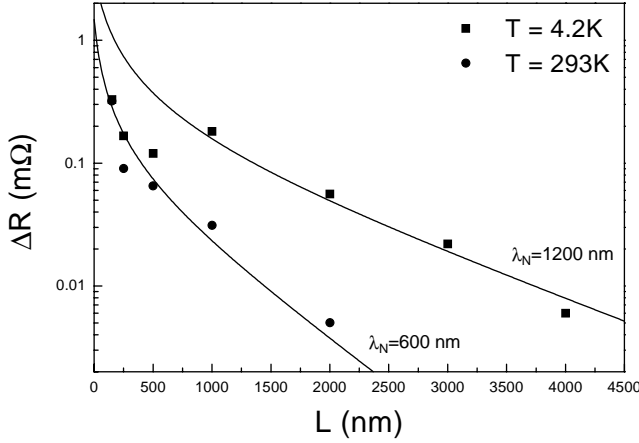
FIG. 9: Dependence of the magnitude of the spin signal ΔR on the Py electrode distance L, measured in the non local geometry for Py/Al/Py spin valves. The solid squares represent data taken at $T = 4.2$ K, the solid circles represent data taken at RT. The solid lines represent the best fits based on equation 12.

of Sec. VI. Note that for the Py/Al/Py spin valve also applies that $M >> 1$ and thus the spin signal ΔR is proportional to the product $\alpha_F \lambda_F$ ($25 < M < 32$). Using Eq. 15, a polarization P for the Py/Al/Py sample with the smallest Py electrode spacing of $L = 250$ nm at $T = 4.2$ K is found to be only 3%: $P = 0.03$.

VIII. SPIN INJECTION USING CO AND NI FERROMAGNETIC ELECTRODES

From Eq. 23 it can be seen that the magnitude of the spin dependent resistance $R_\downarrow - R_\uparrow$ is sensitive to the properties α_F, λ_F and σ_F of the ferromagnet. As $R_\downarrow - R_\uparrow$ enters squared in the spin valve signal ΔR, see Eq. 21, an increase of λ_F with a factor 10 would increase ΔR with a factor 100. We have therefore tried cobalt (Co) and nickel (Ni) as ferromagnetic spin injectors and detectors to increase the magnitude of the spin valve signal, as larger spin relaxation lengths can be expected for these materials.[5,6]

A. Spin accumulation in Co/Cu/Co spin valves

Figure 10a shows a "contact" magneto resistance trace and magnetic switching behavior at RT of a 14×0.5 μm^2 (Co2) electrode of a Co/Cu/Co spin valve device with a Co electrode spacing of 250 nm and Co electrodes of sizes 2×0.8 μm^2 and 14×0.5 μm^2. The "contact" magneto resistance is measured by sending current from contact 5 to 7 and measuring the voltage between contacts 6 and 9 (see Fig. 3). Note that in this geometry the measured voltage is not sensitive to a spin valve signal as only one Co electrode is used in the measurement configuration.

The magneto resistance traces of Fig. 10a indicate a clear switching of the magnetization at 20 mT of the 14×0.5 μm^2 Co2 electrode and is attributed to a local Hall effect produced at the Co/Cu contact area of the Co2 electrode.
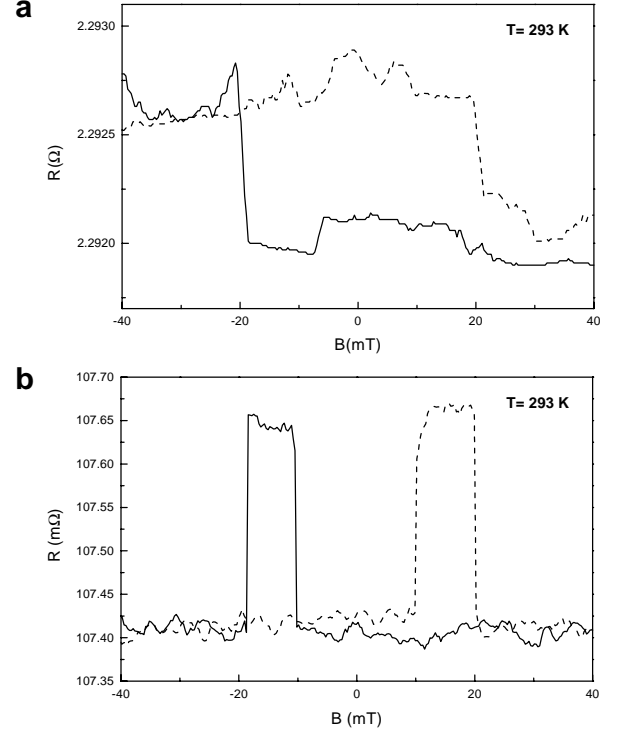

FIG. 10: a, "Contact" magneto resistance trace of the Co2 electrode with size 14×0.5 μm^2. The Hall signal indicates an abrupt magnetization switching of the Co2 electrode. b, The spin valve effect at RT in a Co/Cu/Co device with a Co electrode spacing $L = 250$ nm, using the non local measurement geometry. The solid(dotted) curve corresponds with a negative (positive) sweep direction of the B-field.

Figure 10b shows the spin valve effect at RT for a Co/Cu/Co spin valve device. The magnitude of the spin dependent resistance $\Delta R = 0.25$ $m\Omega$ is slightly smaller than in the Py/Cu/Py spin valve device. At $T = 4.2$ K the signal increases to $\Delta R = 0.8$ $m\Omega$. Using Eq. 12 and the values of σ_N, λ_N for Cu and σ_F for Co (see Sec. V), we obtain $\alpha_F \lambda_F = 0.3$ at RT and $\alpha_F \lambda_F = 0.7$ at $T = 4.2$ K. These obtained values are much smaller than reported for Co in GMR experiments, where $\alpha_F \approx 0.5$ and $\lambda_F = 10 - 60$ nm.[35,51,52,53,54] This discrepancy will be discussed in Sec. IX C.

B. Spin accumulation in Ni/Cu/Ni spin valves

In Fig. 11a and b two "contact" magneto resistance traces of a Ni electrode (Ni1) with size 2×0.5 μm^2 (top curve) and a Ni electrode (Ni2) with size 14×0.15 μm^2 (middle curve) are shown of a Ni/Cu/Ni spin valve de-
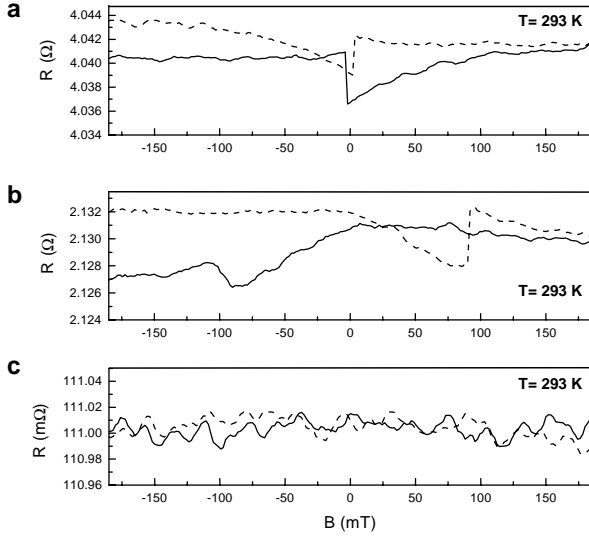
FIG. 11: (a) "Contact" magneto resistance trace (see text) of the Ni1 electrode with size 2×0.5 μm^2. (b) "Contact" magneto resistance trace of the Ni2 electrode with size 14×0.15 μm^2. (c) The spin valve effect of a Ni/Cu/Ni device at RT with a Ni electrode spacing of $L = 500$ nm, using a non local measurement geometry. The solid(dotted) curve corresponds with a negative (positive) sweep direction of the B-field.

vice with a Ni electrode spacing of 500 nm. For the Ni1 contact current is send from contact 1 to 5 and the voltage is measured from contact 4 to 6 (see Fig. 3). For the Ni2 contact current is send from contact 5 to 7 and the voltage is measured from contact 6 to 9. In the magnetic field sweeps of Figs. 11a and 11b a large range can be observed where the magnetization configuration of the Ni electrodes are anti-parallel. However no spin valve signal could be detected within experimental accuracy in the non local measurement geometry at RT as well as at $T = 4.2$ K, as is shown in Fig. 11c (RT). An upper bound on the spin valve signal is found to be $\Delta R < 20$ $\mu\Omega$ at RT as well as at $T = 4.2K$. Using Eq. 12 and the values of σ_N, λ_N for Cu and σ_F for Ni (see Sec. V), we obtain $\alpha_F \lambda_F < 0.3$ at RT as well as at $T = 4.2$ K. These obtained values are also much smaller than reported for Ni in GMR experiments, where $\alpha_F \approx 0.2$ and using the expected $\lambda_F(calc) = 15$ nm.[50,55] This discrepancy will be discussed in Sec. IX C.

We note that the magnetic field in the measurements of Fig. 11 is applied perpendicular to the long axis of the Ni electrodes, showing a more pronounced magnetic switching behavior than an applied magnetic field along the long axis of the Ni electrodes.

IX. SPIN RELAXATION TIMES OF CONDUCTION ELECTRONS IN METALS

In this section we will analyze our obtained spin relaxation times τ_{sf} in Cu and Al from the spin injection experiments in Secs. VI,VII VIII and compare them with theory and previously reported values from CPP-GMR[56], CESR[57], weak localization[58] and superconducting tunneling experiments[7]. The obtained spin polarization and spin relaxation lengths in Py, Co and Ni will be compared with reported values from CPP-GMR experiments.

In CESR experiments the measured electron spin transverse relaxation time T_2 is proportional to the width of the absorption peak at the resonance frequency. Yafet[59] showed that in metals T_2 is equal to the longitudinal spin relaxation time or spin flip time T_1 ($T_1 = \tau_{sf}$). In weak localization and superconducting tunneling experiments the spin orbit scattering time $\tau_{s.o.}$ is determined, with $\tau_{s.o.}$ being defined similarly in both experiments.[60] Spin orbit interaction in weak localization experiments is responsible for destructive interference when electrons are scattered at (nonmagnetic) impurities[58], whereas in the superconducting tunneling experiments it mixes up the spin-up and spin-down quasi-particle density of states, when they are Zeeman-split by an applied magnetic field.[7,61] We make the identification $\tau_{s.o.} = \tau_{sf}$.

A. Discussion of electron spin relaxation in nonmagnetic metals

The fact that a spin can be flipped implies that there is some mechanism which allows the electron spin to interact with its environment. In the absence of magnetic impurities in the nonmagnetic metal, the dominant mechanism that provides for this interaction is the spin-orbit interaction, as was argued by Elliot and Yafet.[59,62] When included in the band structure calculation the result of the spin-orbit interaction is that the Bloch eigenfunctions become linear combinations of spin-up and spin-down states, mixing some spin-down character into the predominantly spin-up states and vice versa.[63] Using a perturbative approach Elliot showed that a relation can be obtained between the elastic scattering time (τ_e), the spin relaxation time (τ_{sf}) and the spin orbit interaction strength defined as $(\lambda/\Delta E)^2$:

$$\frac{\tau_e}{\tau_{sf}} = a \propto (\frac{\lambda}{\Delta E})^2 , \qquad (30)$$

where λ is the atomic spin-orbit coupling constant for a specific energy band and ΔE is the energy separation from the considered (conduction) band to the nearest band which is coupled via the atomic spin orbit interaction constant. Yafet has shown that Eq. 30 is temperature independent[59]. Therefore the temperature dependence of $(\tau_{sf})^{-1}$ scales with the temperature behavior of the resistivity being proportional to (τ_e^{-1}). For

many clean metals the temperature behavior of the resistivity is dominated by the electron-phonon scattering and can to a good approximation be described by the Bloch-Grüneisen relation[64]: $(\tau_{sf})^{-1} \sim T^5$ at temperatures below the Debye temperature T_D and $(\tau_{sf})^{-1} \sim T$ above T_D. Using data from CESR experiments, Monod and Beuneu[65,66] showed that $(\tau_{sf})^{-1}$ follows the Bloch-Grüneisen relation for monovalent alkali and noble metals. In Fig. 12 their results are replotted for Cu and Al, using the revised scaling as applied by Fabian and Das Sarma.[63] In addition we have plotted the obtained data points for Cu and Al at $T/T_D \approx 1$ from our spin injection experiment by calculating τ_{sf} from λ_{sf} (see Sec. IX B below) and using the calculated spin orbit strength parameters from Ref. 65: $(\lambda/\Delta E)^2 = 2.16 \cdot 10^{-2}$ for Cu and $(\lambda/\Delta E)^2 = 3 \cdot 10^{-5}$ for Al.
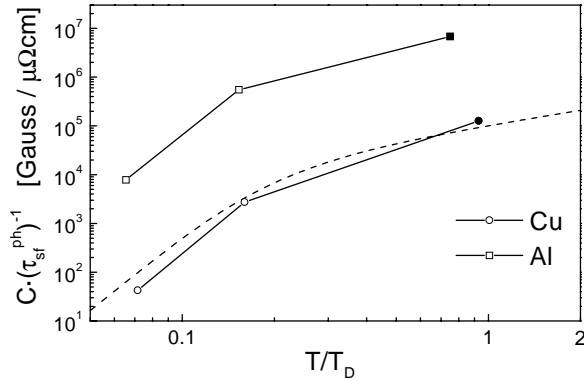

FIG. 12: The (revised) Bloch-Grüneisen plot[63]. The quantity $C \cdot (\tau_{sf}^{ph})^{-1}$ is plotted versus the reduced temperature T/T_D on logarithmic scales. C represents a constant which links $(\tau_{sf}^{ph})^{-1}$ to the (original) plotted width of a CESR resonance peak, normalized by the spin orbit strength $(\lambda/\Delta E)^2$ and the resistivity ρ_D at $T = T_D$: $C = (\gamma(\lambda/\Delta E)^2 \rho_D)^{-1}$. Here $(\tau_{sf}^{ph})^{-1}$ is the phonon induced spin relaxation rate, γ is the Larmor frequency and T_D is the Debye temperature. We used $\rho_D = 1.5 \cdot 10^{-8}$ and $T_D = 315$ K for Cu and $\rho_D = 3.3 \cdot 10^{-8}$ and $T_D = 390$ K for Al.[57,64] The dashed line represents the general Bloch-Grüneisen curve. The open squares represent Al data taken from CESR and the JS spin injection experiment (Refs. 16,67). The open circles represent Cu data taken from CESR experiments (Refs. 68,69,70). The solid square (Al) and circle (Cu) are values from the spin injection experiments described here and Refs. 18,20.

From Fig. 12 it can be seen that for Cu the Bloch-Grüneisen relation is well obeyed, *including* the newly added point deduced from our spin injection experiments at RT ($T/T_D = 0.9$). For Al however the previously obtained data points as well as the newly added point from the injection experiments at RT ($T/T_D = 0.75$) are deviating from the general curve, being about two orders of magnitude larger than the calculated values based on Eq. 30. We note that we cannot extract data for the Bloch-Grüneisen plot shown in Fig. 12 from our spin injection experiments at $T = 4.2$ K, because the impurity (surface) scattering rate is completely dominating the phonon contribution at $T = 4.2$ K.

Fabian and Das Sarma have resolved this discrepancy for Al by pointing out that there can exist so called 'spin-hot-spots' at the Fermi surface of poly valent metals(like Al). Performing an ab initio pseudopotential band structure calculation of Al they showed that the spin flip contribution of these (small) spin-hot-spot areas on the (large) Fermi surface dominate the total spin flip scattering rate τ_{sf}, making it factor 100 faster than expected from the Elliot-Yafet relation.[71,72,73] A simplified reasoning for the occurrence of these spin-hot-spots is that in poly valent metals the Fermi surface can cross the first Brillioun zone making the energy separation ΔE in Eq. 30 between the (conduction) band to the spin orbit coupled band much smaller at these (local) crossings and hence result in a larger spin orbit strength $(\lambda/\Delta E)^2$. Our newly added data point shows that the under estimation of the spin orbit strength also holds for Al at RT ($T/T_D = 0.75$), as can be seen in Fig.12. However it is in excellent agreement with the theoretical predicted value by Fabian[73] as will show below.

B. Quantative analysis of the spin relaxation time τ_{sf} in Cu and Al

Comparing the conductivities and spin relaxation lengths at RT and $T = 4.2$ K we can obtain the impurity and phonon scattering rate and their associated spin relaxation rates. Therefore we can define an impurity spin relaxation ratio $a^{imp} = \tau^{imp}/\tau_{sf}^{imp}$ and an inelastic (phonon) scattering ratio $a^{ph} = \tau^{ph}/\tau_{sf}^{ph}$. Here $(\tau^{imp})^{-1}$ and $(\tau^{ph})^{-1}$ are the impurity and phonon scattering rate and $(\tau_{sf}^{imp})^{-1}$ and $(\tau_{sf}^{ph})^{-1}$ are the impurity and phonon induced spin relaxation rate. From the measured conductivity at $T = 4.2$ K and Eq. 2 we can determine τ^{imp}. Using the Mathiessen rule $(\tau_e)^{-1} = (\tau^{imp})^{-1} + (\tau^{ph})^{-1}$ and the RT conductivity we can determine τ^{ph}. We note that the surface scattering in our samples is dominating the impurity scattering, as the mean free paths of $l_e \approx 60$ nm for both Al and Cu at $T = 4.2$ K are larger than their film thicknesses (50 nm). In the calculation we use the free electron values $N(E_F)_{Cu} = 1.8 \cdot 10^{28}$ states/eV/m^3 and $v_F(Cu) = 1.57 \cdot 10^6$ m/s for Cu[74] and we use $N(E_F)_{Al} = 2.4 \cdot 10^{28}$ states/eV/m^3 and $v_F(Al) = 1.55 \cdot 10^6$ m/s for Al.[75]

The obtained parameters for Cu and Al (τ_{sf}^{imp}, τ_{sf}^{ph}, a^{imp}, a^{ph}) are tabulated in tabel I. From tabel I we see that τ_{sf}^{ph} and a_{ph} for Al at RT are in good agreement with the theoretical values as predicted in the bandstructure calculation by Fabian and Das Sarma.[73] They are also in agreement with the results obtained from CESR experiments and the earlier JS spin injection experiments at temperatures below 90 K. Note that the spin relaxation times are 2 orders of magnitude larger in those earlier experiments due the use of extremely clean samples with

Aluminum (Al)

	τ_{sf}^{imp} [ps]	a_{imp}	τ_{sf}^{ph} [ps]	a_{ph}	Ref.
Theory	-	-	90 [a]	$1.2 \cdot 10^{-4}$ [a]	73
Spin Injection	100	$0.6 \cdot 10^{-4}$	85 [a]	$1.1 \cdot 10^{-4}$ [a]	20
Spin Injection	70	$3.7 \cdot 10^{-4}$	124 [a]	$1.3 \cdot 10^{-4}$ [a]	This work
Spin Injection (JS)	9000	$15 \cdot 10^{-4}$	4000 [b]	$4.8 \cdot 10^{-4}$ [b]	16
CESR	$3000 - 9000$	$9.0 \cdot 10^{-4}$	$1000 - 57000$ [c]	$2.6 \cdot 10^{-4}$ [c]	67,69,73
Anti-weak localization	4-46	$(0.2 - 1.2) \cdot 10^{-4}$	-	-	76,77
Superconducting tunneling	8-160	$(0.1 - 5) \cdot 10^{-4}$	-	-	7,78,79,80

Copper (Cu)

	τ_{sf}^{imp} [ps]	a_{imp}	τ_{sf}^{ph} [ps]	a_{ph}	Ref.
Spin Injection	41	$0.7 \cdot 10^{-3}$	14 [a]	$2.0 \cdot 10^{-3}$ [a]	this work, 18
CESR	$2000 - 9000$	$0.8 \cdot 10^{-3}$	$2000 - 21000$ [d]	$1.1 \cdot 10^{-3}$ [d]	68,69
GMR	4	$19 \cdot 10^{-3}$	-	-	46
Anti-weak localization	5	$1.3 \cdot 10^{-3}$	-	-	76,77
Energy-level spectroscopy	20-80	-	-	-	81

TABLE I: Comparison of spin relaxation times between different experiments. τ_{sf}^{imp} [ps] is the impurity induced spin relaxation time at low temperatures $T \leq 4.2$ K due to surface scattering, dislocations or grain boundaries. τ_{sf}^{ph} [ps] is the phonon induced spin relaxation time at elevated temperatures due to inelastic phonon scattering. For definition of a_{imp} and a_{ph} see text.

[a] For T=293 K
[b] For T=45 K
[c] For a temperature range T=[1..90] K
[d] For a temperature range T=[1..60] K

electron mean free paths of a few tens of micrometers. Also for Cu we see that τ_{sf}^{ph} and a_{ph} at RT are in good agreement with the results obtained from CESR experiments at temperatures below 60 K.

The impurity scattering ratio a^{imp} shows a much bigger spread in values for both Al and Cu. We speculate that this due to the different origin of the impurities in the samples used for the various measurement techniques. For the CESR experiments the impurity scattering is caused by dislocations, whereas for our experiment it is mainly due to surface scattering. In weak-localization and superconducting tunneling experiments the used films are even thinner then our films (few nm), causing additional scattering from grain boundaries in addition to the surface scattering.

We note that for thin films we use it is not possible to realize mean free paths of the order of micrometers as they will always be limited by surface scattering. However the sensitivity of the CESR technique does not allow measurements of τ_{sf}^{ph} below typically 1 ns, whereas the SQUID detection technique used in Ref. 16 does not operate at RT. Therefore spin injection into thin films is rather complementary to the CESR techniques and the JS spin injection experiments in the determining τ_{sf}^{ph} in the temperature range from liquid Helium to RT. Also, the fact that about half of the momentum scattering processes at RT is due to phonon scattering implies that the present obtained results on the spin relaxation lengths in

Al and Cu can be maximally improved by a factor of 2 at RT.

C. Spin injection efficiency of Py, Co and Ni ferromagnets

In addition to the spin-orbit spin scattering in metallic ferromagnets, as described above for nonmagnetic metals, there is spin flip scattering by magnons.[39] In cobalt magnons are nearly absent at low temperatures and only start to compete with the spin orbit spin flip scattering at temperatures higher than $T = 100$ K.[52] The spin flip scattering by magnons has two effects. It will simply add to the spin orbit spin flip scattering rate which reduces the spin relaxation length λ_F of the ferromagnet at higher temperatures. Secondly, it will lower the bulk current polarization of the ferromagnet α_F by changing $\sigma_\uparrow$ and $\sigma_\downarrow$ and in addition by giving rise to a "spin mixing rate" which equalizes the spin-up and spin-down currents in the ferromagnet.[38,39] The presence of spin flip scattering by magnons can therefore lower α_F as well as λ_F at RT.

At low temperatures $(T < 100K)$ and in absence of magnetic impurities an upper estimate can be given for the expected spin relaxation length in Co and Ni due to the spin orbit spin flip scattering only: $\lambda_F = \sqrt{D\tau_e/a}$, where a is taken from spin flip scattering cross-

sections determined by CESR experiments[50,82] and recently from magneto-optic experiments[83]: $a_{Fe} = 1.1 \cdot 10^{-2}$, $a_{Ni} = 1.5 \cdot 10^{-2}$ and $a_{Co} = 4.2 \cdot 10^{-2}$. Using a free electron model, the spin relaxation length λ_{Py} for Py with $\sigma_{Py} = 8.1 \cdot 10^6 \ \Omega^{-1}m^{-1}$ and λ_{Co} for Co with $\sigma_{Co} = 1.7 \cdot 10^7 \ \Omega^{-1}m^{-1}$ have been estimated in this way in Ref. 35: $\lambda_{Py}(calc) \approx 9$ nm and $\lambda_{Co}(calc) \approx 36$ nm at $T = 4.2$ K.[35] Note that λ_F scales linearly with τ_e and thus the conductivity of the ferromagnetic metal. In this respect the reported value of $\lambda_{Co} = 59$ nm in Ref.52 is quite remarkable, because the conductivity of the Co metal ($\sigma_{co} = 6.4 \cdot 10^6$) used in Ref.52 is about 3 times smaller then used to calculate $\lambda_{Co}(calc)$ in Ref.35 ($\sigma_{co} = 1.74 \cdot 10^7$), which makes the expected $\lambda_{Co}(calc) = 13$ nm in the experiment of Ref.52. For Ni we derive an estimate of λ_F using a free electron density of $5.4 \cdot 10^{28} \ m^{-3}$. With $\sigma_{Ni} = 1.6 \cdot 10^7 \ \Omega^{-1}m^{-1}$ and $a_{Ni} = 1.5 \cdot 10^{-2}$ we calculate: $\lambda_{Ni}(calc) = 15$ nm at $T = 4.2$ K.

Because $M > 10$ for all our spin valve samples, we cannot separately determine α_F and λ_F from the magnitude of the spin valve signal ΔR. In table II we therefore give the "spin injection efficiency" $\alpha_F \lambda_F$ together with reported values from GMR experiments. We note that our thin film conductivities for Py, Co and Ni are within a factor 2 of the reported values in the GMR experiments.

	$Ni_{80}Fe_{20}$		Co		Ni	
	4.2 K	RT	4.2 K	RT	4.2 K	RT
$\alpha_F \lambda_F$ MSV	1.2	0.5	0.7	0.3	< 0.1	< 0.1
$\alpha_F \lambda_F$ GMR	3.6 - 4.0[a]	-	4.5 - 27.7[b]	8.1 - 15.5[b]	3[c]	-

TABLE II: Spin injection efficiencies $\alpha_F \lambda_F$ in nm for three different ferromagnetic metals. The data is deduced from the mesoscopic spin valve (MSV) experiments with transparent contacts in a non local geometry using Cu as nonmagnetic metal and compared with results from GMR experiments.

[a] From Refs.35,36,37
[b] From Refs.5,6,51,52,53,54
[c] From Refs.50,55 ($\alpha_{Ni} = 0.2$) and using $\lambda_{Ni}(calc) = 15$ nm

Table II shows that our obtained spin injection efficiency of the Py ferromagnet $\alpha_{Py} \lambda_{Py}$ is in quantative agreement with the values reported in GMR experiments ($\alpha_{Py} = 0.7$, $\lambda_{Py} = 5$ nm), taking into account that our obtained $\alpha_{Py} \lambda_{Py}$ represents a minimal value due to a partially shunting of the injected current by the Cu wire on top of the Py electrodes. The reduction of $\alpha_{Py} \lambda_{Py}$ at RT beyond the ratio 1.8 of the Py conductivies at $T = 4.2$ K and RT could be attributed to magnons lowering α_F at RT.

For the Co and the Ni ferromagnets we observe much smaller spin injection efficiencies $\alpha_F \lambda_F$, being more than 1 order of magnitude smaller than values of $\alpha_F \lambda_F$ obtained in GMR experiments. So the question is, what is causing this rather large reduction of the the spin valve

signal?

First we discuss the possible influences of an existing interface resistance at the Co/Cu and Ni/Cu interfaces. From the resistance measured in a conventional geometry we are able to determine an upper estimate of the (diffusive) interface resistances. For the Co/Cu/Co spin valve of Fig. 10 we find an upper limit for a single Co/Cu interface of 0.4 Ω, whereas for the Ni/Cu/Ni spin valve of Fig. 11 we find for a single Ni/Cu interface 0.6 Ω. We note that the associated interface resistivity ($\approx 5 \cdot 10^{-15} \ \Omega m^2$) values are about 5 times larger than calculated for Co/Cu (specular or diffusive) interfaces[4,84,85,86] and also 5 times larger than values obtained from GMR experiments.[47,51] In case these Co/Cu and Ni/Cu interface resistances are spin dependent, the spin signal would be (largely) increased as the sign of the bulk and interface spin asymmetries of Co, Ni and Cu are found both to be positive[50,85,86,87] ($\alpha_F > 0$ and $\eta > 0$). However this is clearly not observed. In the opposite case of spin independent interface resistances, the interface resistance for each spin channel ($\approx 1 \ \Omega$) will not reduce the measured spin valve signal much as the spin independent interface resistance just adds to the (larger) spin independent resistance of the Cu strip of about 6 Ω (see Sec. VI D eqs. 28 and 29). The spin signal can therefore only be significantly be reduced due to a possible spin flip scattering mechanism at the interface, an effect which has recently been studied in CPP-GMR spin valves.[88,89] The physical origin of this mechanism could be diverse, for instance: surface roughness creating local magnetic fields due to the formation of random domains, a dead magnetic layer of the first few nm of Co or Ni and the formation of anti-ferromagnetic oxides CoO and NiO at the surface during the time in between the Kaufmann sputtering and the Cu deposition. However as we do not have a characterization of the interfacial structure we cannot analyze what could be the most probable cause. We do note that the above mentioned mechanisms could also apply for the Py/Cu interface, however the Py/Cu/Py spin valve data show that their manifestation in these samples is apparently absent or less severe.

Secondly, a change in the bulk properties of the Co and Ni could explain the small spin valve signals. All though in our opinion it is not likely that the bulk spin relaxation length would be subdue to a substantial shortening, a reduction of the polarization α_F in our Co and Ni ferromagnets might occur. In CIP-GMR experiments[90] a strong decrease of more than an order of magnitude in the GMR signal was reported upon changing the base (H_2O) pressure of the in the vacuum chamber from 10^{-8} to 10^{-5} mbar, just before deposition the Co and Cu layers. In our deposition chamber the base pressure is only 10^{-7} mbar, whereas in the experiments e.g. on Co/Ag multilayers[51] the base pressure is of the system is 10^{-8} mbar. However, theoretical work[87] does predict $\alpha_{Co} \approx 0.6$ for Co with a conductivity close to our thin Co film $\sigma_{Co} = 7.3 \cdot 10^6 \ \Omega^{-1}m^{-1}$. We note however that the Co layers in the Co/Cu multilayered nanowires[52] and

the Co/Ag multilayers[51] have a hcp structure, whereas the calculations of Ref. 87 were done on fcc cobalt. Unfortunately we do not know the crystallinity and/or the crystal orientation of our Co films.

X. CONCLUSIONS

We have demonstrated spin injection and accumulation in metallic mesoscopic spin valves with transparent contacts. We have shown that in a conventional measurement geometry the magneto resistance effects of the injecting and detecting contacts can be much larger than the spin valve effect, making it impossible to observe the spin valve effect in a 'conventional' measurement geometry. However, these contact effects can be used to monitor the magnetization reversal process of the spin injecting and detecting contacts. In a non-local measurement geometry we can completely isolate the spin valve effect, as was reported earlier in Ref. 18. Using this geometry we find spin relaxation lengths in Cu of around 1 μm at $T =$ 4.2 K and 350 nm at RT and spin relaxation lengths in Al of around 1.2 μm at $T =$ 4.2 K and 600 nm at RT. The associated spin relaxation times in Al and Cu are in good agreement with theory and values from experiments previously reported in the literature. For the Py material we find spin relaxation lengths and current polarizations in agreement with GMR experiments. However for Co we obtain values of $\alpha_F \lambda_F$ which are up to a factor 40 smaller than their GMR counterpart. For Ni electrodes we are unable to resolve a spin valve signal within the limits of our experimental accuracy, corresponding with $\alpha_F \lambda_F$ at least a factor 10 lower than expected. Finally, we believe that the use of tunnel barriers should make it possible to increase the polarization of the injected current in non-magnetic metals, as we recently have shown.[20,21] This should make it possible to increase the spin signals to about 1 Ω in metals.

[*] Electronic address: jedema@phys.rug.nl

[†] Present address: Department of Applied Physics and Center for Nanomaterials, Eindhoven University of Technology, 5600 MB, The Netherlands.

[1] *Semiconductor Spintronics and Quantum Computation*, edited by D. D. Awschalom, D. Loss and N. Samarth (Springer Verlag, Berlin, 2002).

[2] G. A. Prinz, Science **282**, 1660 (1998).

[3] S. A. Wolf, D. D. Awschalom, R. A. Buhrmann, J. M. Daughton, S. von Molnár, M. L. Roukes, A. Y. Chtchelkanova, D. M. Treger, Science **294**, 1488 (2001).

[4] M. A. M. Gijs and G. E. W. Bauer, Advances in Physics **46**, 285 (1997).

[5] J-Ph. Ansermet, J. Phys.:Condens. Matter **10**, 6027 (1998).

[6] J. Bass, W. P. Pratt Jr., J. Mag. Magn. Mater. **200** 274 (1999).

[7] R. Meservey and P. M. Tedrow, Physics Reports **238**, 173 (1994).

[8] J. S. Moodera, L. R. Kinder, T. M. Wong, and R. Meservey Phys. Rev. Lett. **74**, 3273 (1995).

[9] D. J. Monsma, R. Vlutters, J. C. Lodder, Science **281**, 407 (1998); D. J. Monsma, J. C.Lodder, Th. J. A. Popma, D. Dieny, Phys. Rev. Lett. **74**, 5260 (1995).

[10] W. H. Rippard, R. A. Buhrmann, Phys. Rev. Lett. **84**, 971, (2000).

[11] J. C. Slonczewski, J. Mag. Magn. Mater. **159** L1 (1996).

[12] J. Z. Sun, Phys. Rev. B. **62**, 570 (2000).

[13] J. -E. Wegrowe, D. Kelly, Y. Jaccard, Ph. Guittienne, J.-Ph. Ansermet, Europhys. Lett. **45**, 626 (1999).

[14] E. B. Myers, D. C. Ralph, J. A. Katine, R. N. Louie, R.A. Buhrmann, Science **285**, 867 (1999); J. A. Katine, F. J. Albert, R. A. Buhrman, E. B. Myers, D. C. Ralph, Phys. Rev. Lett. **84**, 3149 (2000).

[15] J. Grollier, V. Cros, A. Hamzic, J. M. George, H. Jaffrès, A. Fert, G. Faini, J. Ben Youssef, H. Legall, Appl. Phys. Lett. **78**, 3663 (2001).

[16] M. Johnson, and R. H. Silsbee, Phys. Rev. Lett. **55**, 1790 (1985).

[17] M. Johnson and R. H. Silsbee, Phys. Rev. B **37**, 5312 (1988); M. Johnson and R. H. Silsbee, Phys. Rev. B **37**, 5326 (1988).

[18] F. J. Jedema, A. T. Filip, B. J. van Wees, Nature **410**, 345 (2001).

[19] F. J. Jedema, M. S. Nijboer, A. T. Filip, B. J. van Wees, Journal of Superconductivity **15** (1), 27 (2002).

[20] F. J. Jedema, H. B. Heersche, A. T. Filip, J. J. A. Baselmans, B. J. van Wees, Nature **416**, 713 (2002).

[21] F. J. Jedema, M. V. Costache, H. B. Heersche, J. J. A. Baselmans, B. J. van Wees, submitted to Appl. Phys. Lett.

[22] J. A. Caballero, C. E. Moreau, W. P. Pratt, Jr., N. O. Birge, IEEE Trans. Mag. **37**, 2111 (2001).

[23] G. Schmidt, D. Ferrand, L. W. Molenkamp, A. T. Filip, B. J. van Wees, Phys. Rev. B **62**, R4790 (2000).

[24] S. Datta, *Electronic transport in mesoscopic systems* (Cambridge University Press, Cambridge, 1995).

[25] A. Fert, and I. A. Campbell, J. de Physique, Colloques **32**, C1-46 (1971).

[26] P. C. van Son, H. van Kempen, and P. Wyder, Phys. Rev. Lett. **58**, 2271 (1987).

[27] T. Valet and A. Fert, Phys. Rev. B **48**, 7099 (1993).

[28] M. Johnson, R. H. Silsbee, Phys. Rev. B **35**, 4959 (1987).

[29] M. Johnson, Phys. Rev. Lett. **70**, 2142 (1993); M. Johnson, Science **260**, 320 (1993).

[30] M. Johnson, J. Appl. Phys. **75**, 6714 (1994).

[31] A. Fert, S. Lee, Phys. Rev. B **53**, 6554 (1996).

[32] S. Hershfield, L. Z. Zhao, Phys. Rev. B **56**, 3296 (1997).

[33] M. B. Stears, J. Mag. Magn. Mater. **5** 167 (1977).

[34] I. I. Oleinik, E. Yu. Tsymbal, D. G. Pettifor, Phys. Rev. B **62**, 3952 (2000).

[35] S. Dubois, L. Piraux, J.M. George, K. Ounadjela, J.L. Duvail, A. Fert, Phys. Rev. B **60**, 477 (1999).

[36] S. D. Steenwyk, S.Y. Hsu, R. Loloee, J. Bass, W.P. Pratt, Jr., J. Mag. Magn. Mater. **170**, L1 (1997).

[37] P. Holody, W. C. Chiang, R. Loloee, J. Bass, W. P. Pratt, Jr., and P. A. Schroeder, Phys. Rev. B **58**, 12230 (1998).

[38] A. Fert, I. A. Campbell, J. Phys. F, **6**, 849 (1976).

[39] A. Fert, J. L. Duvail, T. Valet, Phys. Rev. B, **52**, 6513 (1995).

[40] In our definition τ_{sf} is equal to the spin lattice relaxation time T_1 as used in the Bloch equations.[17] In the Valet-Fert theory $(\tau_{sf})^{VF}$ is different. The difference originates a different expression for $(\lambda_{sf}^2)^{-1}$. In the V-F theory [27] $\lambda_{sf}^2 = (1/D_\uparrow + 1/D\downarrow)^{-1}\tau_{sf}^{VF}$, whereas we derive $\lambda_{sf}^2 = ([N_\downarrow/D_\uparrow(N_\uparrow+N_\downarrow)+N_\uparrow/D_\downarrow(N_\uparrow+N_\downarrow)]^{-1}\tau_{sf}$. In nonmagnetic metals the definition of [27] corresponds therefore to twice the value of our τ_{sf}: $(\tau_{sf})^{VF} = 2\tau_{sf} = 2T_1$.

[41] A. T. Filip, B. H. Hoving, F. J. Jedema, B. J. van Wees, B. Dutta, S. Borghs, Phys. Rev. B **62**, 9996 (2000).

[42] S. F. Lee, W. P. Pratt, Jr., R. Loloee, P. A. Schroeder, J. Bass, Phys. Rev. B **46**, 548 (1992).

[43] F. G. Monzon, M. L. Roukes, J. Magn. Magn. Mater. **198**, 632 (1999).

[44] J. Nitta, T. Schäpers, H. B. Heersche, T. Koga, Y. Sato, H. Takayanagi, Jap. J. Appl. Phys. **41**, 2497 (2002).

[45] Th. G. S. M. Rijks, R. Coehoorn, M.J. M. de Jong and W. J. M. de Jonge, Phys. Rev. B **51**, 283 (1995).

[46] Q. Yang, P. Holody, S.-F. Lee, L. L. Henry, R. Loloee, P. A. Schroeder, W. P. Pratt, Jr., J. Bass, Phys. Rev. Lett. **72**, 3274 (1994).

[47] Q. Yang, P. Holody, R. Loloee, L. L. Henry, W. P. Pratt, Jr., P. A. Schroeder, J. Bass, Phys. Rev. B **51**, 3226 (1995).

[48] M. Johnson, Nature **416**, 809 (2002).

[49] M. Johnson, Semicond. Sci. Technol. **17**, 298 (2002).

[50] C. Vouille, A. Barthélémy, F. Elokan Mpondo, A. Fert, P. A. Schroeder, S. Y. Hsu, A. Reilly, R. Loloee, Phys. Rev. B **60**, 6710 (1999).

[51] S.-F. Lee, Q. Yang, P. Holody, R. Loloee, J. H. Hetherington, S. Mahmood, B. Ikegami, K. Vigen, L. L. Henry, P. A. Schoeder, W. P. Pratt, Jr., J. Bass, Phys. Rev. B **52**, 15426 (1995).

[52] L. Piraux, S. Dubois, A. Fert, L. Beliard, Eur. Phys. J. B **4**, 413 (1998); L. Piraux, S. Dubois, C. Marchal, J.M. Beuken, L. Filipozzi, J. F. Despres, K. Ounadjela, A. Fert, J. Mag. Magn. Mater. **156** 317 (1996).

[53] B. Doudin, A. Blondel, J.-Ph. Ansermet, J. Appl. Phys. **79**, 6090 (1996).

[54] U. Ebels, A. Radulescu, Y. Henry, L. Piraux, K. Ounadjela, Phys. Rev. Lett. **84**, 983 (2000).

[55] H. Kubota, M. Sato, T. Miyazaki, Phys. Rev. B **52**, 343 (1995).

[56] W. P. Pratt, Jr., S.-F. Lee, J. M. Slaughter, R. Loloee, P. A. Schroeder, J. Bass, Phys. Rev. Lett. **66**, 3060 (1991).

[57] C. Kittel, *Introduction to Solid State Physics* (Wiley 7th edition, New York, 1996).

[58] G. Bergmann, Physics Reports **107**, 1 (1984).

[59] Y. Yafet, in *Solid State Physics*, edited by F. Seitz and D. Turnbull (Academic, New York, 1963), Vol. 14.

[60] J. A. X. Alexander, P. M. Tedrow, T. P. Orlando, Phys. Rev. B **34**, 8157 (1986).

[61] P. Fulde, Adv. Phys. **22**, 667 (1973).

[62] R. J. Elliot, Phys. Rev. **96**, 266 (1954).

[63] J. Fabian, S. Das Sarma, J. Vac. Sci. Technol. B **17**, 1708 (1999).

[64] J. Bass in *Metals: Electronic Transport Phenomena*, edited by K. H. Hellwege and J. L. Olsen, Landolt-Börnstein (Springer-Verlag, Berlin, 1982) Group 3, Vol. 15, Part a.

[65] F. Beuneu, P. Monod, Phys. Rev. B **18**, 2422 (1978).

[66] P. Modod, F. Beuneu, Phys. Rev. B **19**, 911 (1979).

[67] D. Lubzens, S. Schultz, Phys. Rev. Lett. **36**, 1104 (1976).

[68] S.Schultz, C. Latham, Phys. Rev. Lett. **15**, 148 (1965).

[69] F. Beuneu, P. Monod, Phys. Rev. B **13**, 3424 (1976).

[70] P. Monod, A. Janossy, J. Low Temp. Phys. **26**, 311 (1977).

[71] J. Fabian, S. Das Sarma, Phys. Rev. Lett. **81**, 5624 (1998).

[72] J. Fabian, S. Das Sarma, J. Appl. Phys. **85**, 5075 (1999).

[73] J. Fabian, S. Das Sarma, Phys. Rev. Lett. **83**, 1211, (1999).

[74] N. W. Ahscroft, N. D. Mermin, in *Solid State Physics* (W.B. Saunders Company, Orlando, 1976).

[75] D. A. Papaconstantopoulos, in *Handbook of the band structure of elemental solids* (Plenum, New York, 1986).

[76] G. Bergmann, Phys. Rev. B **29**, 6114 (1984).

[77] J. M. Gordon, C. J. Lobb, M. Tinkham, Phys. Rev. B Rap. Comm. **28**, 4046 (1983).

[78] R. Meservey, P. M. Tedrow, R. C. Bruno, Phys. Rev. B **11**, 4224 (1975).

[79] C. Grimaldi, P. Fulde, Phys. Rev. Lett. **77**, 2550 (1996).

[80] D. J. Monsma, S. S. P. Parkin, Appl. Phys. Lett. **77**, 720 (2000).

[81] J. R. Petta, D. C. Ralph, Phys. Rev. Lett. **87**, 266801-1, (2001).

[82] P.Monod, S. Schultz, J. Physique **43**, 393 (1982).

[83] B. Koopmans, M. van Kampen, J. T. Kohlhepp, W. J. M. de Jonge, Phys. Rev. Lett. **85**, 844 (2000).

[84] P. M. Levy, Solid State Phys. **47**, 367 (1994).

[85] K. M. Schep, J. B. A. N. van Hoof, P. J. Kelly, G. E. W. Bauer, J. E. Inglesfield, Phys. rev. B **56**, 10805 (1997); see also K. Schep Ph.D. thesis, Delft University of Technology (1997).

[86] K. Xia, P. J. Kelly, G. E. W. Bauer, I. Turek, J. Kudrnovsky, V. Drchal, Phys. Rev. B **63**, 064407 (2001).

[87] E. Yu. Tsymbal, D.G. Pettifor, Phys. Rev. B **54**, 15314 (1996).

[88] W. Park, D. V. Baxter, S. Steenwyk, I. Moraru, W.P. Pratt, Jr., J. Bass, Phys. Rev. B **62**, 1178 (2000).

[89] C. H. Marrows, B.J. Hickey, Phys. Rev. B **63**, 220405-1 (2001).

[90] W. F. Egelhoff, Jr., P. J. Chen, C. J. Powell, M.D. Stiles, R. D. McMichael, C.-L. Lin, J. M. Sivertsen, J. H. Judy, K. Takano, A. E. Berkowitz, T. C. Anthony, J.A. Brug, J. Appl. Phys. **79**, 5277 (1996).